Journal of
Applied Crystallography
ISSN 1600-5767

Real space crystallography of a complex metallic alloy: high-angle annular dark-field scanning transmission electron microscopy of o-Al_4(Cr,Fe)

Roberto Gaspari, Rolf Erni, Yadira Arroyo, Magdalena Parlinska-Wojtan, Julia Dshemuchadse, Carlo A. Pignedoli, Daniele Passerone, Patrik Schmutz and Alessandra Beni

J. Appl. Cryst. (2014). **47**, 1026–1031

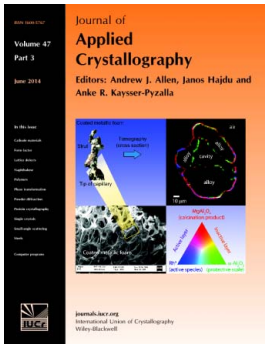

Journal of
Applied Crystallography
ISSN 1600-5767

Received 23 January 2014
Accepted 16 April 2014

Real space crystallography of a complex metallic alloy: high-angle annular dark-field scanning transmission electron microscopy of o-Al_4(Cr,Fe)

Roberto Gaspari,[a,b] Rolf Erni,[c] Yadira Arroyo,[c] Magdalena Parlinska-Wojtan,[c]‡ Julia Dshemuchadse,[d] Carlo A. Pignedoli,[a] Daniele Passerone,[a] Patrik Schmutz[e] and Alessandra Beni[e]*

[a]nanotech@surfaces Laboratory, Empa, Swiss Federal Laboratories for Materials Science and Technology, Ueberlandstrasse 129, Duebendorf 8600, Switzerland, [b]D3-Computation, Italian Institute of Technology, via Morego 30, Genoa 16163, Italy, [c]Electron Microscopy Center, Empa, Swiss Federal Laboratories for Materials Science and Technology, Ueberlandstrasse 129, Duebendorf 8600, Switzerland, [d]Laboratory of Crystallography, Department of Materials, ETH Zurich, Wolfgang-Pauli-Strasse 10, Zurich 8093, Switzerland, and [e]Laboratory for Joining Technologies and Corrosion, Empa, Swiss Federal Laboratories for Materials Science and Technology, Ueberlandstrasse 129, Duebendorf 8600, Switzerland. Correspondence e-mail: alessandra.beni@empa.ch

High-angle annular dark-field scanning transmission electron microscopy (HAADF STEM) has been performed along the low-index zone axes of the o-Al_4(Cr,Fe) complex metallic alloy to obtain a real-space representation of the crystal structure and to elucidate the material's inherent structural disorder. By comparing experiments with multislice STEM simulations, the model previously suggested by X-ray diffraction is further refined to provide a new set of positions and occupancies for the transition metal atoms. *Pmnb* is suggested as the new space group for the o-Al_4(Cr,Fe) phase. A nonperiodic layer-type modulation, averaged out in bulk diffraction methods, is detected, corroborating the need for complementing bulk diffraction analysis with real-space imaging to derive the true crystal structure of Al_4(Cr,Fe).

1. Introduction

Complex metallic alloys (CMAs) form stable intermetallic phases characterized by large unit cells, containing hundreds of atoms and often found as crystalline approximants of quasicrystals (Dubois, 2005; Dubois *et al.*, 2011). The characterization of these intermetallics is generally demanding owing to their complex crystal structure as well as to some inherent degree of disorder caused by the presence of split occupancies and vacancies within the cluster-like arrangement (Steurer & Deloudi, 2009; Dshemuchadse *et al.*, 2011). The o-Al_4(Cr,Fe) CMA phase exhibits excellent corrosion resistance at very low pH (1–2) and has therefore a potentially wider application range than other commercial Al alloys (Beni *et al.*, 2011; Dubois *et al.*, 2011; Ott *et al.*, 2014; Ura-Binczyk *et al.*, 2011). The enhanced corrosion resistance of this phase is ascribed to the passivating effect given by Cr. The reactivity of this intermetallic has been the subject of a detailed study under ultra high vacuum (UHV) as well as in ambient conditions, and the material has been found to exhibit an ordered oxide growth during the first stage of oxidation in UHV and an anisotropic behavior of the oxidation and of the corrosion properties relative to the three low-index [100], [010] and [001] surface terminations (Parle *et al.*, 2013; Smerdon *et al.*, 2009). Nevertheless, the absence of an accurate bulk structural model with all the split occupancies resolved is hindering the development of a representation for the surface structure and a detailed mechanism of its oxidation/corrosion.

The structure of the o-Al_4(Cr,Fe) phase with composition $Al_{80.6}Cr_{10.7}Fe_{8.7}$ (at.%) was characterized by X-ray diffraction (XRD) by Deng *et al.* (2004). In the model proposed by Deng *et al.* (2004) (hereafter called the 'D' model), the crystal was reported to belong to the *Immm* space group with unit-cell parameters $a = 12.5$, $b = 12.5$, $c = 30.5$ Å and 306 atoms per unit cell, with a large number of split or partially occupied sites. A more recent study by Bauer and co-workers on o-Al_4(Cr,Fe) with composition $Al_{79.1}Cr_{17.8}Fe_{3.1}$ (at.%) led to an improved model (hereafter called the 'B1' model) combining XRD and neutron diffraction results (Bauer *et al.*, 2009; Bauer, 2010). The neutron study allowed the resolution of certain Cr and Fe sites that are not distinguishable by XRD. Some noticeable differences between the B1 and the D model were observed, mainly in the occupancy of the transition metal (TM) positions and in the presence of an additional atomic position in the asymmetric unit introduced in the B1 model, *i.e.* Fe24, according to the denomination used by Bauer (2010).

‡ Present address: Center for Microelectronics and Nanotechnology, University of Rzeszow, Ulica Pigonia 1, 30-959 Rzeszow, Poland.

Although the B1 model was initially given the same symmetry and unit cell as predicted by the D model, a recent analysis of previously ignored supposed superlattice reflections unveiled the presence of a doubling of the unit cell along the **b** direction, resulting in a reduced crystal symmetry described by the *Pmm*2 space group (Bauer *et al.*, 2013) (hereafter the B2 model). From the analysis of the diffuse phenomena occurring along **c***, the new structure was assumed to be composed of large lamellar '(a, b, c)' and '(a, $2b$, c)' domains occurring with irregular lateral distribution. However, detailed information about these lamellar domains and their domain walls is still missing.

With this work, we aim to determine the occupancy of the transition metal positions for the o-Al_4(Cr,Fe) phase and to characterize the domains and domain wall distribution *via* real-space crystallography, by studying the local, *i.e.* not averaged, crystal structure using high-angle annular dark-field scanning transmission electron microscopy (HAADF STEM) (Abe, 2011).

HAADF STEM has been successfully applied in the past as an atomic number sensitive (Z-contrast) imaging technique to provide direct atomic information about the projected crystal structure and the local atomic organization of quasicrystalline phases (Abe *et al.*, 2003, 2004; Yan *et al.*, 1998). In this paper, we demonstrate the ability of HAADF STEM to characterize the local cluster configuration and to elucidate the inherent disorder of the orthorhombic Al_4(Cr,Fe) CMA phase by inspection of the crystal structure along the three orthogonal zone axes [100], [010] and [001], thus proposing a new structural model where the positions and occupancies of the Cr and Fe transition metal (TM) atoms have been obtained by a direct fit of the model to the experimental result.

The combination of the 'B1' Al positions (*Immm*) with the newly determined TM substructure yields the space group *Pmnb* for this phase. The validity of this space group for the o-Al_4(Cr,Fe) complex metallic alloy is corroborated by the extinctions observed in the XRD pattern.

2. Experimental

2.1. Sample preparation

An o-Al_4(Cr,Fe) single crystal with composition $Al_{79.1}Cr_{17.8}Fe_{3.1}$ (at.%) was grown at the Department of Earth and Environmental Sciences, Ludwig Maximilians University of Munich, using the Czochralski method under argon atmosphere (Bauer & Gille, 2011). Its structure, its composition and the presence of defects were subsequently characterized, respectively, by XRD, electron probe microanalysis (EPMA) and X-ray topography.

The availability of single crystals allowed us to prepare three TEM samples cut along the three major zone axes, namely [010], [001] and [100].

Lamellae suitable for high-resolution HAADF STEM investigations were obtained by metallographic sample preparation and subsequent ion milling.

2.2. HAADF STEM experiments and simulations

The STEM investigations were carried out using a JEOL JEM2200fs microscope with a spherical aberration of 1.0 mm. The convergence semi-angle of the electron probe was set to 10.8 mrad, which, for a defocus of about −50 nm and a finite effective source size, provides a spatial resolution of about 0.2 nm. HAADF STEM images were recorded with an inner detection angle of 100 mrad and with a low beam current and a fast acquisition time to minimize potential radiation damage. To improve the image contrast and to reduce the experimental noise, averaged structural unit-cell information was derived by template matching and averaging using the *MacTempas* software (Bodnarchuk *et al.*, 2013; Rossell *et al.*, 2009). Standard deviation maps of the averaged structure provided information about the reliability of this procedure and on the proper choice of the repeat unit.

Preliminary STEM simulations were performed using an *ad hoc* developed computational procedure (see §3 for further details).

Multislice STEM simulations were carried out using the *xHREM* software (version 3.6; HREM Research, Higashimastuyama, Japan). The HAADF collection angle was set to 100–210 mrad. The electron probe was defined by a 10.8 mrad convergence angle together with a third-order spherical aberration and a defocus of 1 mm and −50 nm, respectively. A Gaussian blurring, reflecting the spatial incoherence of the beam, of 0.2 nm (full width at 1/e) was applied to match the experimental resolution (Dwyer *et al.*, 2008). Images were calculated with a step size of 0.08 nm. The HAADF STEM images were calculated for a large range of thicknesses up to 75 nm, showing no substantial differences of the features of interest. The simulated images in §3 are calculated for 50 nm for the [100] and the [010] zone-axis orientation and for 48.8 nm for [001], corresponding to 40, 20 and 16 unit cells. The thickness of the calculated model crystals was chosen according to experimentally measured thickness values using the log-ratio technique (Malis *et al.*, 1988). Thickness values of around 50 nm turned out to be useful, particularly for assessing the variation of the stacking disorder within the sample and to be able to identify it as such.

3. Results and discussion

Fig. 1(a) displays a noise-filtered STEM image along the [100] zone axis, showing the coexistence of two different patterns, emphasized by lines: one is characterized by a 'zigzag' structure and the other by a 'cross' pattern, also seen as a 'double zigzag' (light blue lines). The 'zigzag' pattern extends regularly over large areas of the crystal, while the 'cross' pattern appears only in narrow domains perpendicular to the [001] direction. Red (A) and green (B) tiles can be used to visualize the origin of the 'zigzag' pattern. A and B tiles indicate rows that are mirrored with respect to each other, with the B tile shifted with respect to the row defined by the A tile by b/2 along the [010] direction. In our analysis, we suggest that the cross pattern originates from an A* tile, which is shifted with

respect to the A tile by $b/4$ along the [010] direction. Similarly, B* tiles can be defined. In general, the lamella-type domains consist of B/B* or A/A* mixtures of variable ratio, *i.e.* because of the finite thickness of the TEM sample there is a continuous range of lamellae where the pure 'zigzag' and the ideal 'cross' patterns represent the extremes (see Fig. 1*a*). The presence and nonperiodicity of the lamellar structure is particularly evident in the incoherently formed bright-field STEM image of Fig. 1(*c*) where the nonperiodic modulations are visible over a long range. This is in agreement with the findings of Bauer *et al.* (2013).

We now focus our attention on the widest domain characterized by the 'zigzag' pattern, by relating the STEM image to the available models based on diffraction studies. Fig. 1(*b*) shows a superposition of the TM sites retrieved by the B1 and D models on the experimental STEM image. Aluminium atoms are not considered in the analysis because their low atomic number implies a small contribution in the HAADF STEM image with respect to the TM atoms, and thus we assume that they provide a nearly constant background contribution. As can be seen in Fig. 1(*b*), all the intensity maxima in the STEM image correspond to TM sites for both the B1 and the D model. However, some of the positions that are considered symmetrically equivalent in the B1 and D models based on *Immm* symmetry are associated with zones displaying non-equivalent brightness in the STEM image. This is the case, for instance, for Cr10 sites, which, if equivalent, would give rise to a cross-shaped pattern, while a precise modulation of their occupancy leads in our case to the observed 'zigzag' feature.

The HAADF STEM observations explain, in real space, the hypothesis of Bauer *et al.* (2013) that the unit cell is actually twice as large in the *b* direction compared with the first model proposed by Deng having *Immm* symmetry. Moreover, the modulation of the Cr10 site occupancy leads to the violation of the centrosymmetrical *Immm* space group.

An additional issue is the Fe24 position, which is predicted in the model of Bauer *et al.* (2013) but which is absent in the model of Deng. In the regions characterized by the presence of the 'zigzag' pattern, this position is confirmed by the HAADF STEM data. However, we find a modulation of the intensity maxima for the different Fe24 sites as well, which according to the B1 model should be equivalent. Hence, this observation reveals a systematic variation in the occupancy of Fe24 sites, which leads to the globally observed pattern. Similarly to what was found for Cr10, this modulation breaks the *Immm* symmetry. In their XRD refinement, Bauer *et al.* (2013) proposed *Pmm*2 as the space group of the crystal. However, the absence of mirror symmetry planes perpendicular to the [001] and [010] directions in the [100] STEM images, which is due to the violation of the equivalence of different Fe24 and Cr10 sites, is not compatible with the *Pmm*2 space group.

Starting from the available crystal models, D and B1, we performed a refinement of the structure and of the occupancies of the TM sites, with the goal of reproducing by simulations the experimental STEM images of the 'double zigzag' domains. The occupancy of the TM sites was fitted according to an incoherent imaging model, where the HAADF STEM image intensity $I(x, y)$ at position (x, y) is

$$I(x, y) \propto (P * \zeta)(x, y), \tag{1}$$

with a real object function $\zeta(x, y) = \sum_i \alpha_i Z_i^2 \delta(x - x_i, y - y_i)$, α_i and Z_i being the atom occupancy and the atomic number associated with the ith position, respectively. δ is the Dirac delta distribution, while $P(x, y)$ describes the intensity profile of the electron probe, which is approximated by a Gaussian. The exponent in Z_i^2 arises from our assumption of pure Rutherford scattering, and * refers to the convolution operation. For incoherent imaging, both the object function $\zeta(x, y)$ and the probe function $P(x, y)$ are real functions. A Gaussian probe function $P(x, y)$ with standard deviation 0.2 nm was used. Moreover, α_i were only allowed to vary in the parameter space {0, 0.25, 0.5, 0.75, 1}, in order to reduce the computational burden of the calculations and avoid overfitting the experimental results. o-Al_4(Cr,Fe) displays a columnar

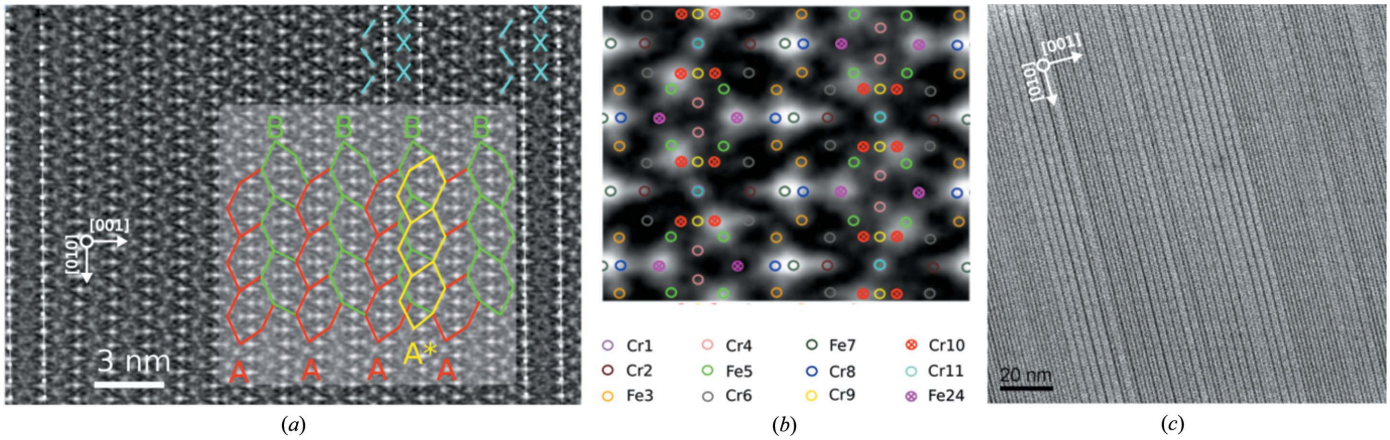

(*a*) (*b*) (*c*)

Figure 1
(*a*) Noise-filtered STEM image viewed along the [100] zone axis. The light blue lines in the right upper corner underline the 'zigzag' and 'cross' patterns, while the A, B and A* tiles highlight the proposed origin of the two motives. (*b*) Superposition of the B1 and D models on the experimental STEM image. Positions Fe24 and Cr10, responsible for the *Immm* symmetry breaking, are highlighted using a crossed circle representation (pink and red). (*c*) Bright-field STEM image viewed along the [100] zone axis.

Table 1
Transition metal positions and their occupancy factors refined according to the HAADF STEM characterization.

The atomic positions are given with respect to space-group symmetry *Pmnb* (No. 62).

No.	Atom	*x*	*y*	*z*	Occupancy
1	Cr1	0.250000	0.375000	0.750000	0.25
2	Cr2*a*	0.250000	0.125000	0.105600	1.00
3	Cr2*b*	0.250000	0.125000	0.394400	1.00
4	Fe3*a*	0.250000	0.027900	0.534600	1.00
5	Fe3*b*	0.250000	0.222100	0.965400	1.00
6	Fe3*c*	0.250000	0.222100	0.534600	1.00
7	Fe3*d*	0.250000	0.027900	0.965400	1.00
8	Cr4*a*	0.250000	0.177350	0.750000	1.00
9	Cr4*b*	0.250000	0.072652	0.750000	1.00
10	Fe5*a*	0.250000	0.472600	0.322102	1.00
11	Fe5*b*	0.250000	0.277400	0.177898	1.00
12	Fe5*c*	0.250000	0.277400	0.322102	1.00
13	Fe5*d*	0.250000	0.472600	0.177898	1.00
14	Cr6*a*	0.250000	0.471700	0.887800	0.75
15	Cr6*b*	0.250000	0.278300	0.887800	0.75
16	Cr6*c*	0.250000	0.278300	0.612200	0.75
17	Cr6*d*	0.250000	0.471700	0.612200	0.75
18	Fe7*a*	0.074235	0.375000	0.987500	1.00
19	Fe7*b*	0.074235	0.375000	0.512498	1.00
20	Cr8*a*	0.250000	0.375000	0.038600	1.00
21	Cr8*b*	0.250000	0.375000	0.461400	1.00
22	Cr9*a*	0.250000	0.223800	0.250000	0.50
23	Cr9*b*	0.250000	0.026200	0.250000	0.50
24	Cr10*a*	0.071731	0.026700	0.204600	0.25
25	Cr10*b*	0.071731	0.223300	0.204600	0.75
26	Cr10*c*	0.071731	0.223300	0.295400	0.25
27	Cr10*d*	0.071731	0.026700	0.295400	0.75
28	Cr11	0.137435	0.125000	0.250000	0.75
29	Fe24*a*	0.061539	0.125000	0.642902	0.25
30	Fe24*b*	0.061539	0.125000	0.857098	0.75

structure with some atoms having identical or nearly identical positions when projected onto given planes. In particular, this occurs for all low-index planes of the crystal, and therefore the analysis of one single STEM image is not sufficient to decouple the contribution provided by atoms arranged perpendicularly to the plane of imaging. For this reason, in this work, two of the three HAADF STEM images recorded along the major orthogonal zone axes were used for the structural refinement, namely the [100] and the [010] axes. [001] was used afterwards to validate the goodness of the fit by comparing the simulated [001] image with the experimental one.

Since the HAADF STEM image intensity is dominated by the contribution of the TM atoms, Al atoms have only been considered as a source of background, and their occupancies have not been re-fitted. The positions of Al atoms have been taken from the B1 model (*Immm*) and replicated in the **b** direction in order to obtain the correct unit-cell size. Lattice parameters were also taken from Bauer (2010). We did not introduce new TM sites since all the peaks in the STEM image are found to be originated by TM positions of the B1 and D models (the chemical identity of the Cr and Fe atoms has been adopted from the B1 model as well) (Bauer, 2010). Nevertheless, both the Cr10 and the Fe24 sites were split and renamed as Cr10*a*, Cr10*b*, Fe24*a*, Fe24*b*, in order to allow for a modulation of the site occupancies compatible with the observed intensity pattern in the [100] projection. The crystal orbit for the new TM subsystem only, induced by the splitting of the Fe24 and Cr10 positions, was retrieved by using the *Materials Studio* suite (version 6.1; Accelrys Inc., San Diego, CA, USA) and was found to be *Pmnb* (with *Pmnb* used as the nonstandard setting of *Pnma*, No. 62). As shown in Table 1, other positions that were equivalent in the B1 model become inequivalent in the refined STEM model, and the number of atoms in the asymmetric unit of the system increases from 13 (B1 model) to 30.

The optimization strategy for the occupancies of the TM positions is explained in what follows. As a first step, one unit cell of the *Pmnb* crystal model is superimposed on the experimental [100] (see Fig. 1*a*) and [010] STEM images, which display clear and distinct intensity peaks. The occupancy α_i of the ith TM position is varied between 0 and 1 until the best local fit between experimental and simulated images is found, that is until the sum of the intensity deviations at (x_m, y_m) in the [010] and [100] planes, $|I_{\rm exp}(x_m, y_m) - I_{\rm sim}(x_m, y_m)|_{[010]} + |I_{\rm exp}(x_m, y_m) - I_{\rm sim}(x_m, y_m)|_{[100]}$, is the smallest.

(x_m, y_m) represents the position of the ith TM atom projected onto the image plane ([010] or [100]), while $I_{\rm exp}$ and $I_{\rm sim}$ correspond, respectively, to the normalized experimental and simulated intensity. $I_{\rm sim}$ is determined directly using equation (1), while $I_{\rm exp}$ corresponds to the normalized image contrast determined as reported in §2.2. The fitting procedure is repeated independently for each TM site, in order to obtain a set of optimized $\{\alpha_i\}$. Iteratively, starting from the $\{\alpha_i\}$ obtained, the fitting procedure is repeated to get a new set $\{\alpha_i'\}$, until $\{\alpha_i\} = \{\alpha_i'\}$. The iterative procedure used ensures that the final set of $\{\alpha_i\}$ corresponds to a minimum, in the parameter space, of the overall intensity deviation, defined as $\sum_i[|I_{\rm exp}(x_i, y_i) - I_{\rm sim}(x_i, y_i)|_{[010]} + |I_{\rm exp}(x_i, y_i) - I_{\rm sim}(x_i, y_i)|_{[100]}]$.

As expected, the Cr10 and Fe24 sites display an intensity modulation, which can be quantified by the different occupancy parameters for Cr10*a*, Cr10*c*, Fe24*a* (0.25) and Cr10*b*, Cr10*d*, Fe24*b* (0.75). Because of the finite size of the electron probe, the occupancy of these sites influences the intensity at other neighboring positions. This can be appreciated by inspection of the Fe5 positions, which, although characterized by identical occupancies, are associated with a slightly different intensity, according to their proximity to highly (or lowly) occupied Cr10 sites.

The samples investigated in the studies of Deng and Bauer and in this manuscript belong to the same orthorhombic phase. The experimental composition of Deng's samples retrieved by EPMA is $Al_{80.6}Cr_{10.7}Fe_{8.7}$ (at.%) (EPMA), while the one used for our characterization and Bauer's is $Al_{79.1}Cr_{17.8}Fe_{3.1}$ (at.%) (EPMA). It has to be noted that the TM contents in the two considered samples (Deng and Bauer/Gaspari) are, respectively, 19.4 and 20.9 at.%, and are thus not dramatically dissimilar, whereas the Cr/Fe ratio changes substantially. Despite the fact that the Cr/Fe ratio is substantially different in the two samples (Deng and Bauer/Gaspari), they are isostructural and belong to the orthorhombic phase.

Because of the proximity of the atomic numbers of Cr and Fe, X-ray diffraction and STEM imaging cannot discriminate Cr and Fe sites, and thus the occupation of the TM sites by Fe

and Cr cannot be determined. In our STEM study, the occupation of the TM sites by Fe and Cr is taken directly from the B1 model, that is the one derived by the neutron characterization performed by Bauer using the $Al_{79.1}Cr_{17.8}Fe_{3.1}$ (at.%) sample and reported by Bauer (2010) to have a calculated composition of $Al_{79.7}Cr_{15.5}Fe_{4.8}$ (at.%).

After the STEM refinement, a different computed composition is obtained, *i.e.* $Al_{79.9}Cr_{10.6}Fe_{9.5}$ (at.%). The computed TM concentration (20.1 at%) is in good agreement with the experimental one (20.9 at.%), while there is a discrepancy with the Cr/Fe ratio. The good agreement between the simulated and experimental STEM images reported in our manuscript indicates that the position of the TM is correct but that the occupation of the TM sites by Fe and Cr should be reconsidered in future neutron diffraction refinements, in order to improve the agreement between the computed and experimental Cr/Fe ratio.

A proposition for the new crystal space group can be made by building a new unit cell that comprises the TM atomic positions retrieved above with the crystal orbit *Pmnb* and the Al atomic positions given by the *Immm* model (B1). The *Materials Studio* suite was used to retrieve the space group for the new unit cell, which was found to be *Pmnb* as well (tolerance of 0.12 Å), as expected from combining the TM (*Pmnb*) with the Al atomic positions (*Immm*). This finding is not in agreement with the results of the B2 model reported by Bauer *et al.* (2013), and this difference is explained by the fact that HAADF STEM allowed us to unequivocally resolve the TM atomic position and occupancy through real-space crystallography, thus reducing the complex data refinement into two simpler steps. The new space group is in agreement with a possible symmetry reduction from the original *Immm* (No. 71) space group, according to the reasoning reported below.

By a symmetry reduction from the *Immm* (No. 71) space group, the *Pmnm* (No. 59, standard *Pmmn*) space group is obtained. Doubling the lattice parameters may lead to the *Pmnb* (No. 62, standard *Pnma*) space group if *b* is doubled or to the *Pmm*2 (No. 25) space group when *a* or *b* or *c* are doubled. This is the operation done during the first step of the refinement, when the positions of the TM were retrieved.

A complete XRD refinement is, however, necessary to fully reconcile our findings with the previous crystal models and provide the final atomic positions and occupancies of the Al atoms.

Using this new unit cell, we performed multislice STEM simulations. The results are shown in Fig. 2 and display an excellent agreement between experiments and simulations for all three orientations [100], [010] and [001]. The simulation for the B2 model is also reported (Fig. 2*c*). This clearly shows that, despite the uncertainty of the Al positions, the refinement of the TM positions substantially improved the existing structure model of o-Al_4(Cr,Fe).

Fig. 2 reports also the relevant symmetry elements of the *Pmnb* space group superimposed on the three simulated images.

In summary, we carried out a high-resolution HAADF STEM characterization of the o-Al_4(Cr,Fe) phase of the Al–Cr–Fe complex metallic alloy with composition $Al_{79.1}Cr_{17.8}$-

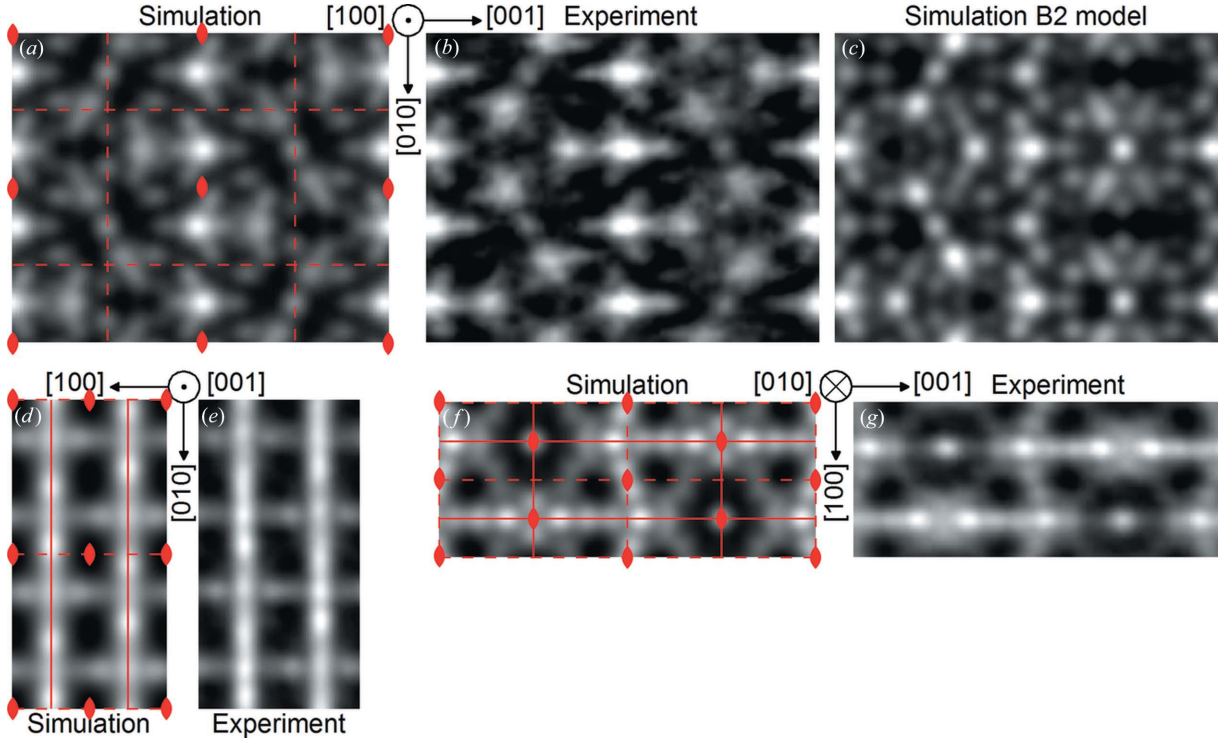

Figure 2
Comparison between experimental (exp) STEM images and multislice STEM simulations (sim). Along [100]: (*a*) sim, (*b*) exp and (*c*) simulation of the B2 model; along [001]: (*d*) sim and (*e*) exp; along [010]: (*f*) sim and (*g*) exp. The relevant symmetry elements for the *Pmnb* space group are superimposed in the simulated images.

$Fe_{3.1}$ (at.%) along the three major zone axes by comparing experiments and simulations using an *ad hoc* routine. This allowed us to perform a real-space crystallographic study with the unequivocal determination of the positions and occupancy values of the transition metal atoms. Using this information, a new unit cell was built considering the retrieved TM atomic positions and occupancies and the Al set already available from diffraction experiments. By the analysis of the symmetries within the new unit cell, a new space group was thus proposed for the o-Al_4(Cr,Fe) phase. The new space group is not in agreement with the previous models retrieved by X-ray and neutron diffraction and thus can be considered an improved model for this phase.

Our results showed that performing real-space crystallography using HAADF STEM and being sensitive only to the TM position allowed the complexity of the structural analysis to be reduced.

Our findings serve as a basis for future bulk investigations, which address the full crystal structure, including the positions and occupancies of the Al atoms. In addition to that, our real-space characterization allowed us to confirm that the crystal is constituted by lamellar domains, which are related to a stacking disorder that occurs nonperiodically along the [001] and the [100] directions.

Dr Birgitta Bauer and Professor Peter Gille of LMU München are acknowledged for providing the single crystals and for sharing their data before publication. Dr Marta D. Rossell is acknowledged for providing support in analyzing the STEM and electron diffraction data. This work was supported by the Swiss National Science Foundation under the contract 200021-129511. Part of the work was developed within the framework of a project financed by the European Network of Excellence on Complex Metallic Alloys 'CMA' (contract No. NMP3-CT-2005-500140) and the European Integrated Centre for the Development of New Metallic Alloys and Compounds 'C-MAC' (http://www.eucmac.eu). The authors acknowledge the VIU IT (STP 3-1-01), the VIL Gender Mainstreaming of 'CMA' NoE and the EMPA Internal Research Program for financial support.

References

Abe, E. (2011). *Scanning Transmission Electron Microscopy*, edited by S. J. Pennycook & P. D. Nellist, pp. 583–614. New York: Springer.
Abe, E., Pennycook, S. J. & Tsai, A. P. (2003). *Nature*, **421**, 347–350.
Abe, E., Yan, Y. & Pennycook, S. J. (2004). *Nat. Mater.* **3**, 759–767.
Bauer, B. (2010). PhD thesis, Ludwig-Maximilians-Universität, Munich, Germany.
Bauer, B. & Gille, P. (2011). *Z. Anorg. Allg. Chem.* **637**, 2052–2058.
Bauer, B., Pedersen, B. & Frey, F. (2013). *Aperiodic Crystals*, edited by S. Schmid, R. L. Withers & R. Lifshitz, pp. 163–170. Dordrecht: Springer.
Bauer, B., Pedersen, B. & Gille, P. (2009). *Z. Kristallogr.* **224**, 109–111.
Beni, A., Ott, N., Ura-Bińczyk, E., Rasinski, M., Bauer, B., Gille, P., Ulrich, A. & Schmutz, P. (2011). *Electrochim. Acta*, **56**, 10524–10532.
Bodnarchuk, M. I., Erni, R., Krumeich, F. & Kovalenko, M. V. (2013). *Nano Lett.* **13**, 1699–1705.
Deng, D. W., Mo, Z. M. & Kuo, K. H. (2004). *J. Phys. Condens. Matter*, **16**, 2283–2296.
Dshemuchadse, J., Jung, D. Y. & Steurer, W. (2011). *Acta Cryst.* B**67**, 269–292.
Dubois, J. M. (2005). *Useful Quasicrystals*, pp. i–xx. Singapore: World Scientific.
Dubois, J. M., Belin-Ferré, E. & Feuerbacher, M. (2011). *Complex Metallic Alloys: Fundamentals and Applications*. Weinheim: Wiley-VCH.
Dwyer, C., Erni, R. & Etheridge, J. (2008). *Appl. Phys. Lett.* **93**, 021115.
Malis, T., Cheng, S. C. & Egerton, R. F. (1988). *J. Electron Microsc. Technol.* **8**, 193–200.
Ott, N., Beni, A., Ulrich, A., Ludwig, C. & Schmutz, P. (2014). *Talanta*, **120**, 230–238.
Parle, J. K., Beni, A., Dhanak, V. R., Smerdon, J. A., Schmutz, P., Wardé, M., Barthés-Labrousse, M. G., Bauer, B., Gille, P., Sharma, H. R. & McGrath, R. (2013). *Appl. Surface Sci.* **283**, 276–282.
Rossell, M., Erni, R., Asta, M., Radmilovic, V. & Dahmen, U. (2009). *Phys. Rev. B*, **80**, 024110.
Smerdon, J., Parle, J., McGrath, R., Bauer, B. & Gille, P. (2009). *Z. Kristallogr.* **224**, 13–15.
Steurer, W. & Deloudi, S. (2009). *Crystallography of Quasicrystals*. Berlin, Heidelberg: Springer.
Ura-Binczyk, E., Homazava, N., Ulrich, A., Hauert, R., Lewandowska, M., Kurzydlowski, K. J. & Schmutz, P. (2011). *Corros. Sci.* **53**, 1825–1837.
Yan, Y., Pennycook, S. & Tsai, A. (1998). *Phys. Rev. Lett.* **81**, 5145–5148.